Supporting Information

Overlimiting current by iodide electrode oxidation in aqueous media: an electrogenerated iodine interphase with positively charged channels stimulating *in situ* electrokinetic iodide transport

Sehyeok Ki[#a], Anseong Park[#b], Won Bo Lee[b], YongJoo Kim*[c], Jinho Chang*[ad]

[a] Department of Chemistry and Research Institute for Convergence of Basic Science, Hanyang University, Seoul, 04763, Republic of Korea

[b] School of Chemical and Biological Engineering, Seoul National University, Seoul, 08826, Republic of Korea

[c] Department of Materials Science and Engineering, Kookmin University, Seoul, 02707, Republic of Korea

[d] Department of HY-KIST Bio-convergence, Hanyang University, Seoul, 04763, Republic of Korea

[#] S.K. and A.P. contributed equally to this work

Table of Contents

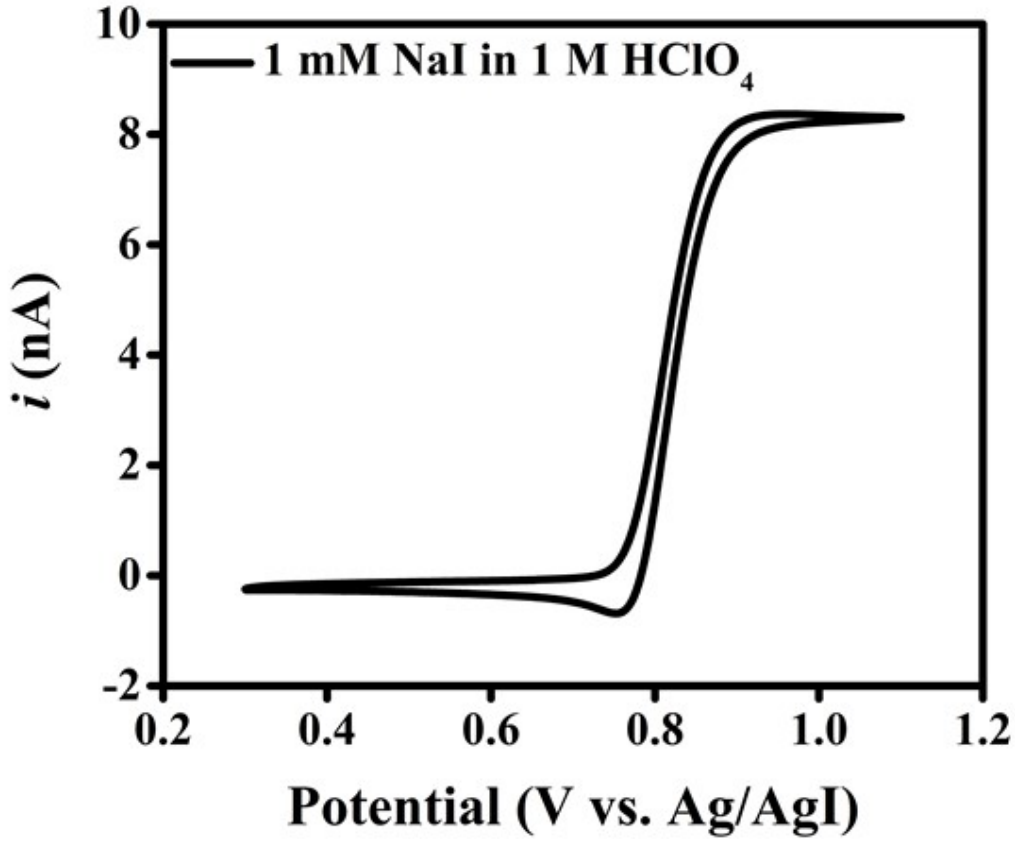

Figure S1. CV obtained using a Pt UME at 0.02 V/s in an aqueous 1 M $HClO_4$ solution containing 1 mM NaI.

Note S1. The voltammetric electrode reaction process associated with the electro-oxidation of I^- in an aqueous solution with low concentration of I^-.

The thorough study of the voltammetric electrode reaction process in aqueous solutions containing the low concentration of I^- ($\leq$ 20 mM) through the rotating ring disk electrode (RRDE) analysis was previously reported from our group.[1]

In the stated previous article (see Figure 1a and the description in the corresponding article), we found that I^- was initially electro-oxidized to soluble I_3^- on the disk electrode, while the electrogenerated I_3^- was collected until the disk potential was positively biased to 0.53 V (vs. Ag/AgCl), where the disk current reached at the quasi limiting value. Then, the disk current abruptly increased while the ring current was found to be decreased as the disk potential was further positively biased due to the electro-oxidation of I_3^- to non-mass transferrable I_2.

Based on the observed RRDE voltammogram, the quasi limiting current in Figure 1a of this article was associated with electro-oxidation of I^- to I_3^- at the diffusion governed condition, and therefore, could be theoretically estimated through the well-known equation (Eq. 2 of this manuscript) described in elsewhere.[2]

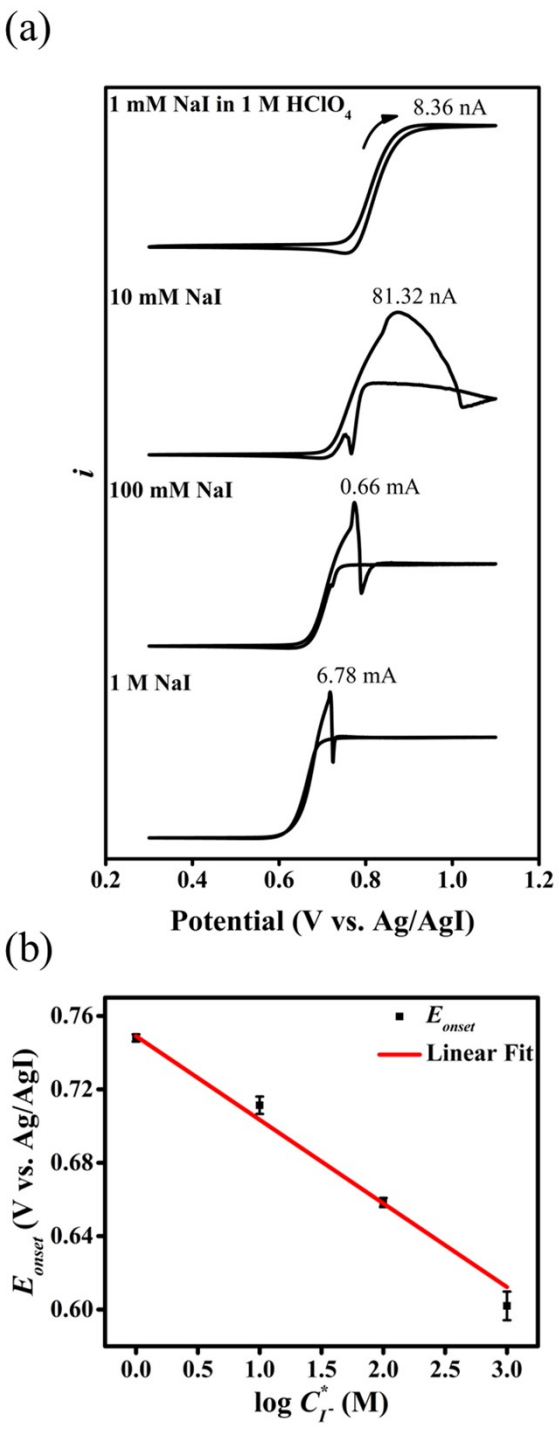

Figure S2. (a) CVs at 0.02 V/s obtained using a Pt UME in aqueous solutions containing 1 M $HClO_4$ with different $C^*_{I^-}$. (b) The corresponding E_{onset} vs. $logC^*_{I^-}$ plot estimated from the CVs in the solutions with the corresponding $C^*_{I^-}$.

Note S2. The detailed description of the finite element analysis for I_3^-/I_2 half-redox reaction using a Pt UME under the diffusion-governed condition.

Figure S3 shows the 2D axial domain and boundaries for finite element analysis, which describes the electro-oxidation of I_3^- on the Pt UME. Three different boundaries were delineated: black, red, and blue. First, B1 represents the bulk solution where the concentration of I_3^- was constant. B2 represents an electrically insulating UME sheath. Finally, B3 corresponds to the electrode with a radius of 12.5 μm.

Two equations were coupled and solved to investigate electrode oxidation of I_3^- to I_2 in the electroneutrality domain. The flux of *i* species, J_i, was obtained by solving the Nernst-Planck equation (S1) considering only diffusion in the entire domain.

$$J_i = -D_i \nabla C_i \tag{S1}$$

here, D_i is the diffusion coefficient of *i* chemical species. $D_{I_3^-}$ and D_{I_2} are assumed to be the same as D_{I^-}. In addition, the electrode kinetics were determined by the Butler-Volmer relation[3] and the electro-oxidation of I_3^- was considered to be Nernstian. Table S3 lists the summarized domain and boundary conditions for the finite element analysis.

The abovementioned equations were solved within the domain using the electroanalysis module of the COMSOL Multiphysics software (ver. 6.0). Analyses were conducted under time-dependent conditions.

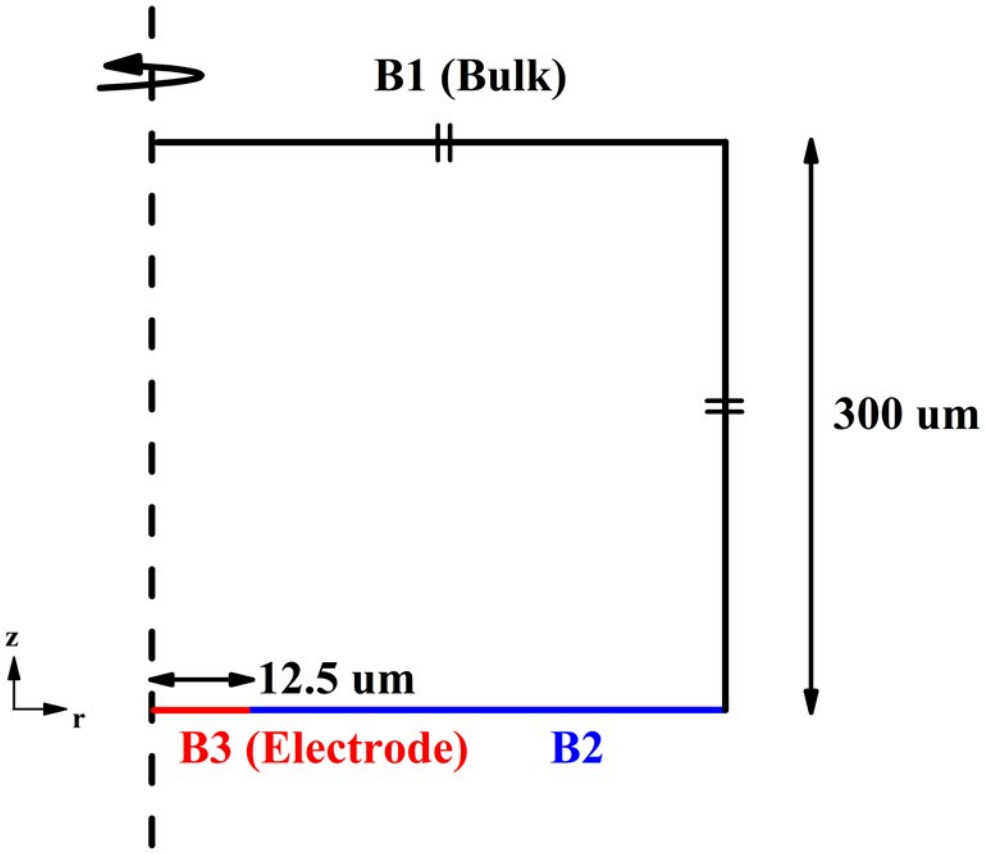

Figure S3. The description of the domain and boundaries for the finite element analysis, as described in Note S2.

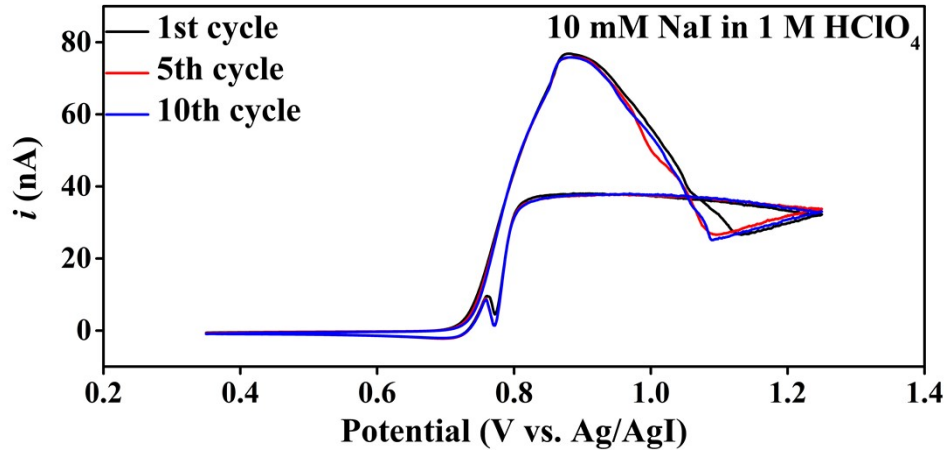

Figure S4. The multi-cycles CVs obtained using a Pt UME at 0.02 V/s in an aqueous solution containing 10 mM NaI with 1 M $HClO_4$, showing 1st (black), 5th (blue), and 10th (red) cycle, respectively.

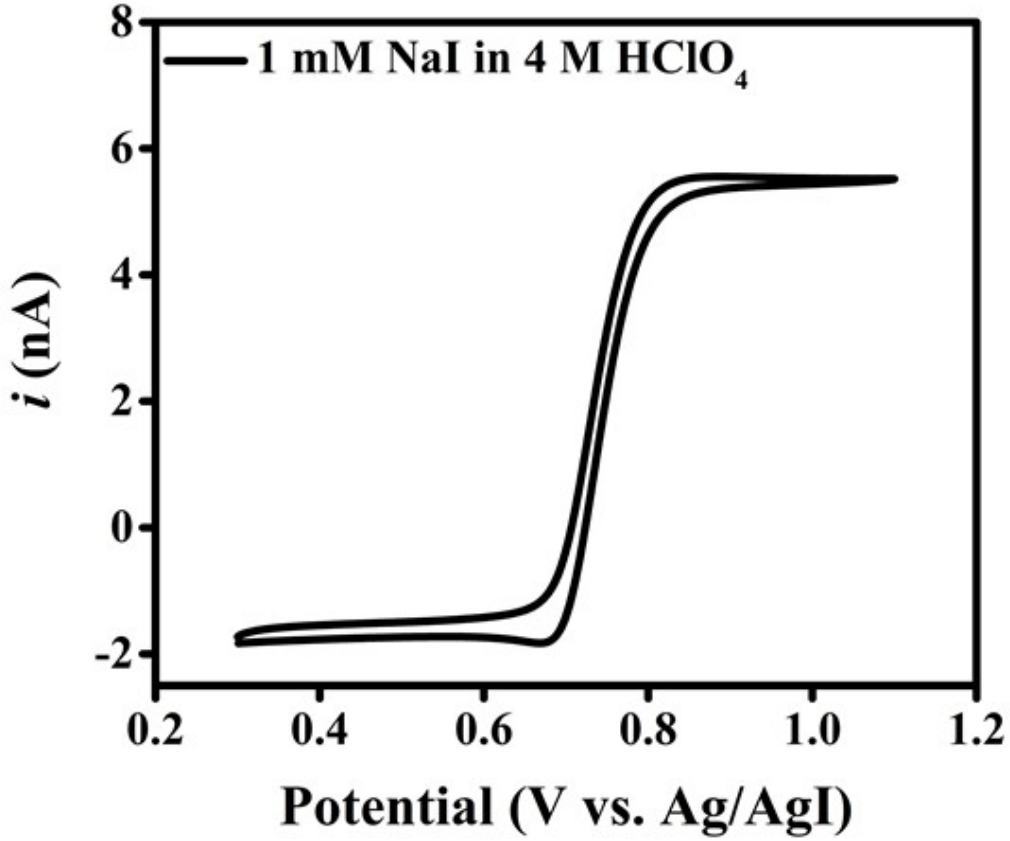

Figure S5. CV obtained using a Pt UME at 0.02 V/s in an aqueous solution containing 1 mM NaI + 4 M $HClO_4$.

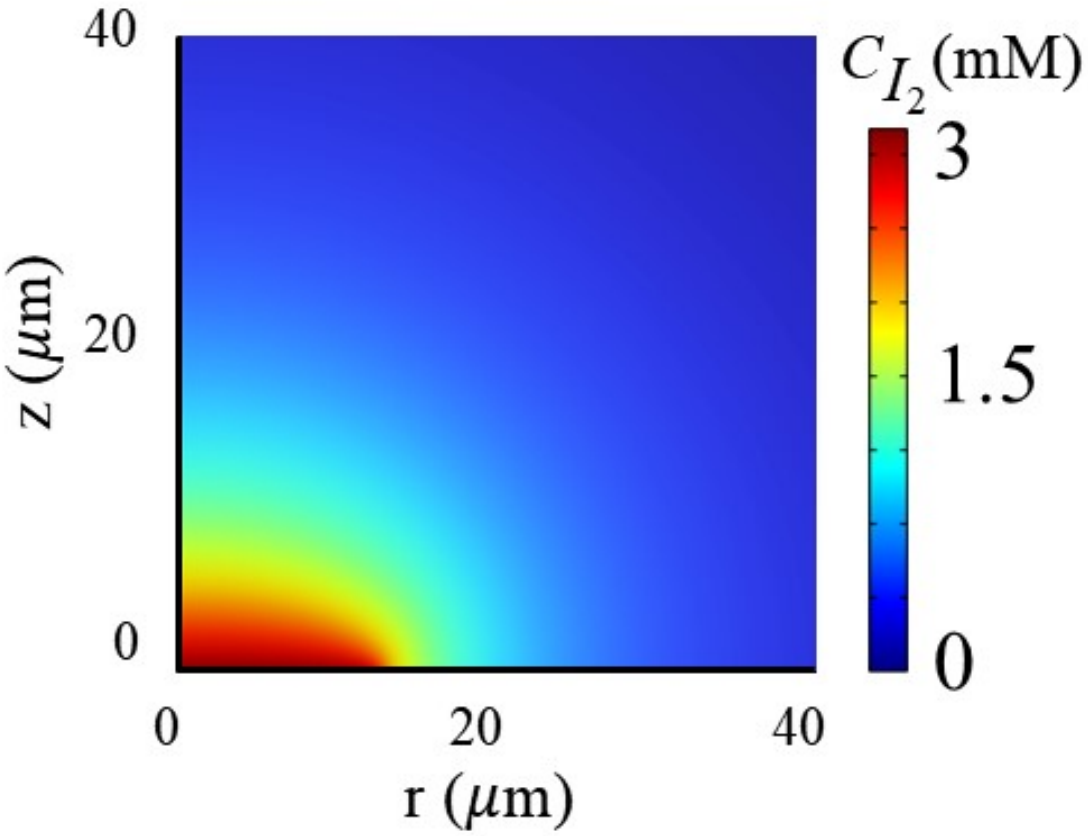

Figure S6. The contour plot of C_{I_2} obtained from the finite element analysis when the oxidative current increases to 29.5 nA due to the electro-oxidation of I_3^-.

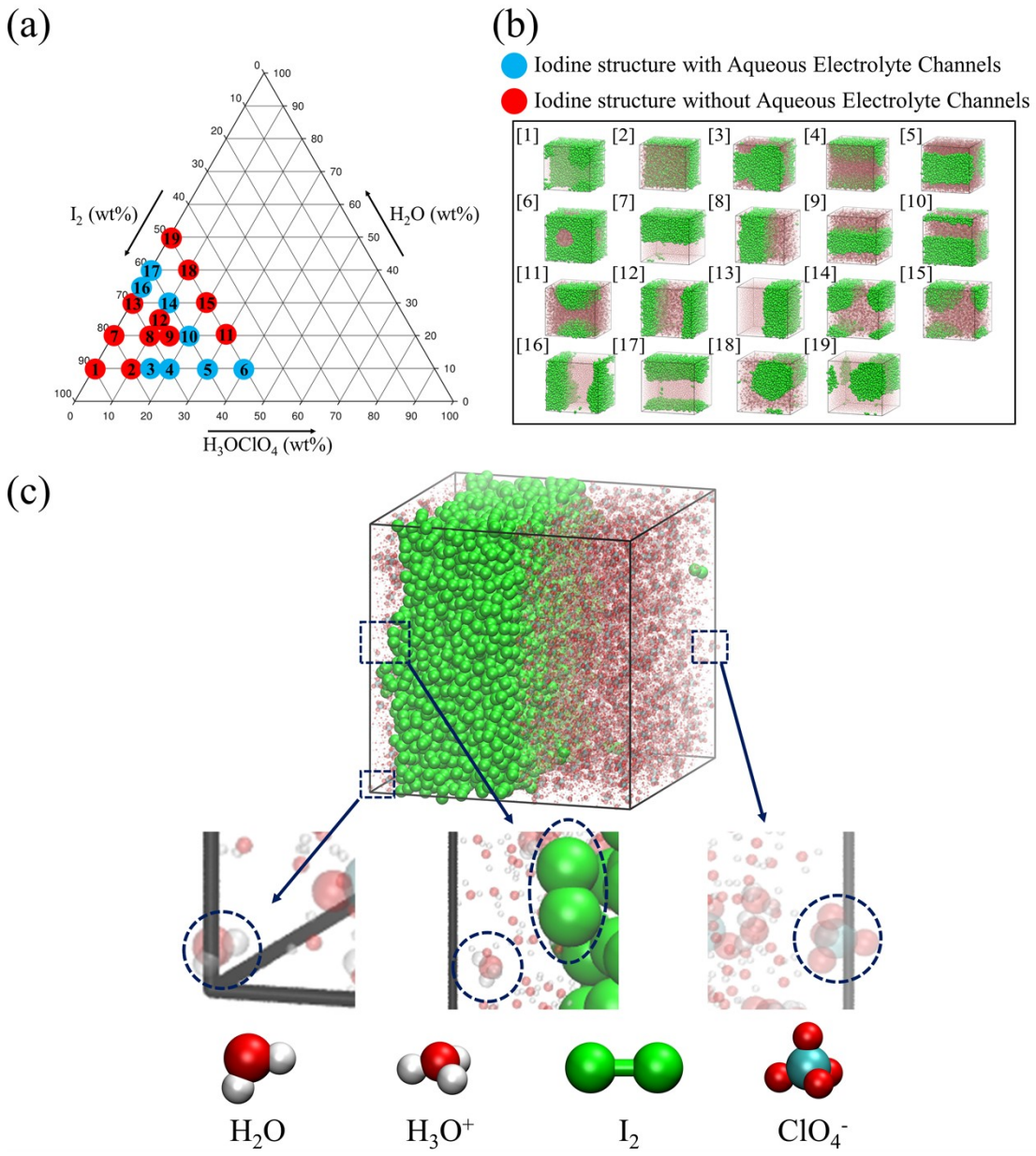

Figure S7. (a) The phase diagrams of I_2 interfacial structures with/without I^--channels as blue and red circles, respectively, at various weight percentages of H_2O, I_2, and $(H_3O)^+ClO_4^-$ estimated from (b) the corresponding MD simulation results; the phases of the iodine structures at the designated numbers were estimated from the MD results with the matched numbers. (c) The representative unit cell and its enlarged region are surrounded by dotted rectangle to show each molecule used in the simulation.

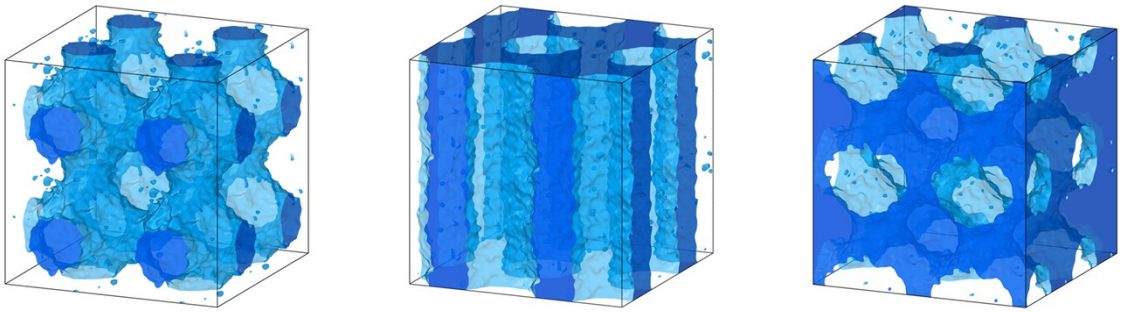

Figure S8. The visualized electrolyte channels from the expanded iodine structures, which are shown as representatives of the porous iodine structure with electrolyte channels in Figure 3b.

Note S3. The detailed description of the finite element analysis for electrokinetic transport of I^- through the model channel.

Figure S9 shows the domains and boundaries of the finite element analysis. The domain illustrates the simplified model I^- channel in the $I_2(H^+)_n$ interfacial domain. Three different boundaries delineated the domains, which are marked in black, red, and blue. The boundary B1 corresponds to the interface between the channel and the bulk solution where the concentrations of both iodide and its counter ions maintain their bulk concentration levels. The boundary B2 represents the wall of the model channel with a certain surface charge density (σ_{Ch}). The boundary B3 corresponds to the electrode where I^- is oxidized and its rate is governed by its mass transfer.

The various equations were fully coupled and solved to investigate the transport of I^- through the model channel. Poisson's equation (Equation S2) was used to solve an electrical potential (ϕ) in the model channel domain.

$$\nabla^2 \cdot \left(- \varepsilon_0 \varepsilon_r \phi \right) = F \sum_i C_i z_i \tag{S2}$$

here, ε_0 is the vacuum permittivity (8.85×10^{-12} F/m) and ε_r is the relative permittivity of the domain, which is 78 for liquid water. F is the Faraday constant (96485 C/mol). C_i and z_i are the concentrations and charges of the chemical species, i. The flux of i, J_i, was obtained using the Nernst-Planck equation (S3).

$$J_i = - D_i \nabla C_i - z_i \frac{D_i}{RT} F C_i \nabla \phi + C_i u \tag{S3}$$

here, R is the molar gas constant (8.314 J/mol · K) and T is the temperature (293.15 K). Finally, the fluid flow u was solved using the Navier-Stokes equation to consider convection-type transport.

$$\rho(u \cdot \nabla)u = -\nabla p + \mu\nabla^2 u + F\sum_i (z_i C_i)\nabla\phi \quad \text{(S4)}$$

here, ρ and μ are the density and the dynamic viscosity of the solution, respectively, which corresponds to 998 kg/m^3 and 0.001 Pa · S for liquid water, respectively. p is the pressure. The incompressible flow condition was applied when solving the Navier-Stokes equation.

$$\rho\nabla \cdot u = 0 \quad \text{(S5)}$$

In the analysis, D_{I^-} and D of its counter anion were set to 1.75 × 10^{-5} cm^2/s. In addition, other parameters were used as variables in the analysis: the channel width (w_{Ch}), the channel length (l_{Ch}), σ_{Ch}, and the concentration of I$^-$ within the model channel ($C_{I^-,Ch}$). The above equations were fully coupled and solved under steady-state conditions using the Tertiary Current Distribution and Laminar Flow modules in COMSOL Multiphysics (ver. 6.0). The current due to oxidation of I$^-$ on the electrode was estimated from the inward flux of I$^-$ (J_{I^-}) at B3 by the following equation. In Equation S6, n is the stoichiometric number of electrons involved in the electrode reaction, which was assumed to be 1 for the analysis.

$$i = nF\int_0^{w_{Ch}} J_{I^-}\, dr \quad \text{(S6)}$$

In addition, electric flux density, $J_{Electric}$, was calculated as follows:

$$J_{Electric} = \epsilon_0 \phi \tag{S7}$$

Table S4 lists the boundary conditions for solving the coupled equations.

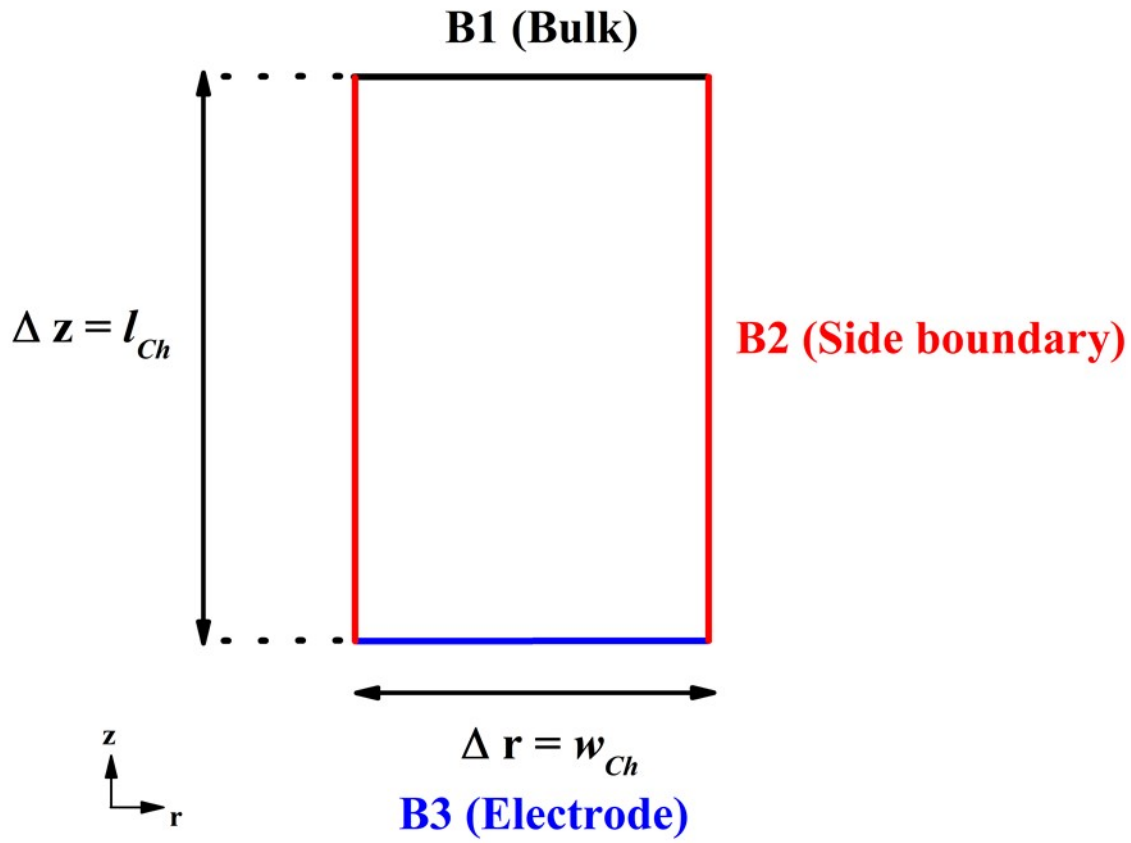

Figure S9. The simplified model channel with the 2D domain for the finite element analysis.

Note S4. The simulated electrokinetic transport of I^- through the model channel with a neutral surface charge at $\Delta\phi$ = +3 V.

Figure S10a shows J_{I^-} along the distance from the electrode to the top of the channel [$d(z)$] at $\Delta\phi$ = 0 V, and therefore, the entire J_{I^-} was associated with diffusion through the channel. The corresponding C_{I^-} profile in Figure S10b shows that I^- was completely depleted only at the electrode surface, and C_{I^-} linearly increased to the bulk concentration of I^- (i.e., 10 mM) as $d(z)$ increased. In contrast to the above case, $\Delta\phi$ could affect the electro-oxidation of I^- significantly. Figure S10c shows the ϕ profile along $d(z)$ at $\Delta\phi$ = 3 V, and ϕ almost linearly decreased as $d(z)$ increased to approximately 200 nm, and reached 0 V at $d(z)$ = 300 nm. The induced electric-flux density (J_{Electric}), which represents the electric-field strength, is shown as a function of $d(z)$ in Figure S10d; the equation for J_{Electric} is described in Note S3. The curve shows that the electric field was strongly driven within the model channel; $d(z)$ for the effectively induced electric field was approximately 200 nm from the electrode, and J_{Electric} drastically decreased as $d(z)$ increased to 300 nm. Because of the strongly induced electric field through the channel, migration of I^- can largely contribute to J_{I^-}. Figure S10e shows J_{I^-} associated with diffusion and migration through the channel. I^- was mainly transported via migration until $d(z)$ became 200 nm from the electrode, and its extent at the electrode was approximately 6 times higher than that via diffusion through the channel, as shown in Figure S10a. At $d(z)$ > approximately 250 nm, J_{I^-} associated with migration decreases, while the diffusional flux increases, and eventually the two fluxes become the same at $d(z)$ = 300 nm. Lastly, Figure S10f shows C_{I^-} as a function of $d(z)$ at $\Delta\phi$ = +3 V. I^- almost depleted in the

channel along $d(z)$ of approximately 200 nm from the electrode, where its electrokinetic transport was the dominant mass transfer phenomena. As noted in Note S3, J_{I^-} associated with convection was also calculated by the analysis. However, its contribution to the total J_{I^-} was negligible compared to that associated with diffusion and migration. Therefore, we only plotted J_{I^-} associated with diffusion and migration, as shown in Figure S10.

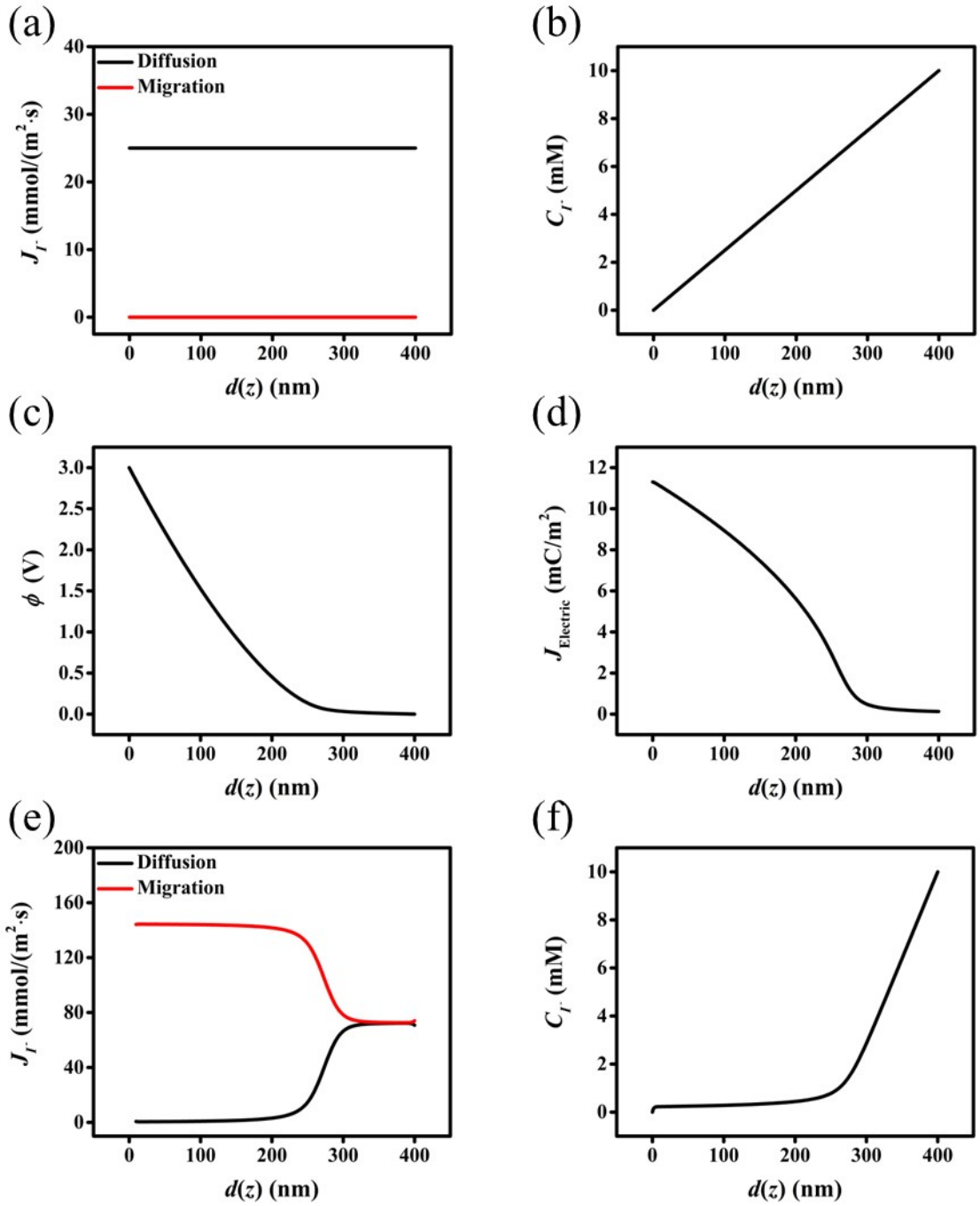

Figure S10. (a) J_{I^-} associated with diffusion (black) and migration (red). (b) C_{I^-} vs. $d(z)$ at $\Delta\phi$ = 0 V. (c) ϕ. (d) J_{Electric} (e) J_{I^-} associated with diffusion (black) and migration (red). (f) C_{I^-} vs. $d(z)$ at $\Delta\phi$ = 3 V; z-axis from the electrode to the top of the channel, as described in Figure S9.

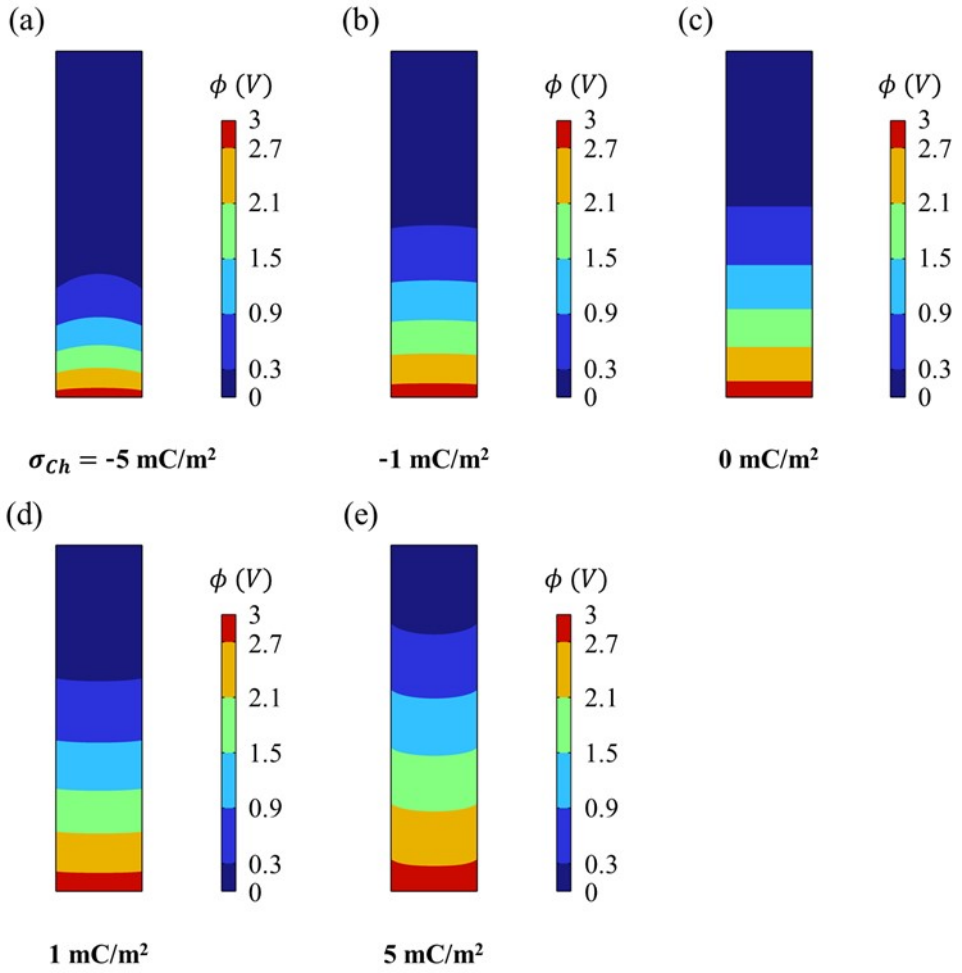

Figure S11. The contour plots of ϕ through the model channel at σ_{Ch} = (a) -5, (b) -1, (c) 0, (d) 1, and (e) 5 mC/m^2.

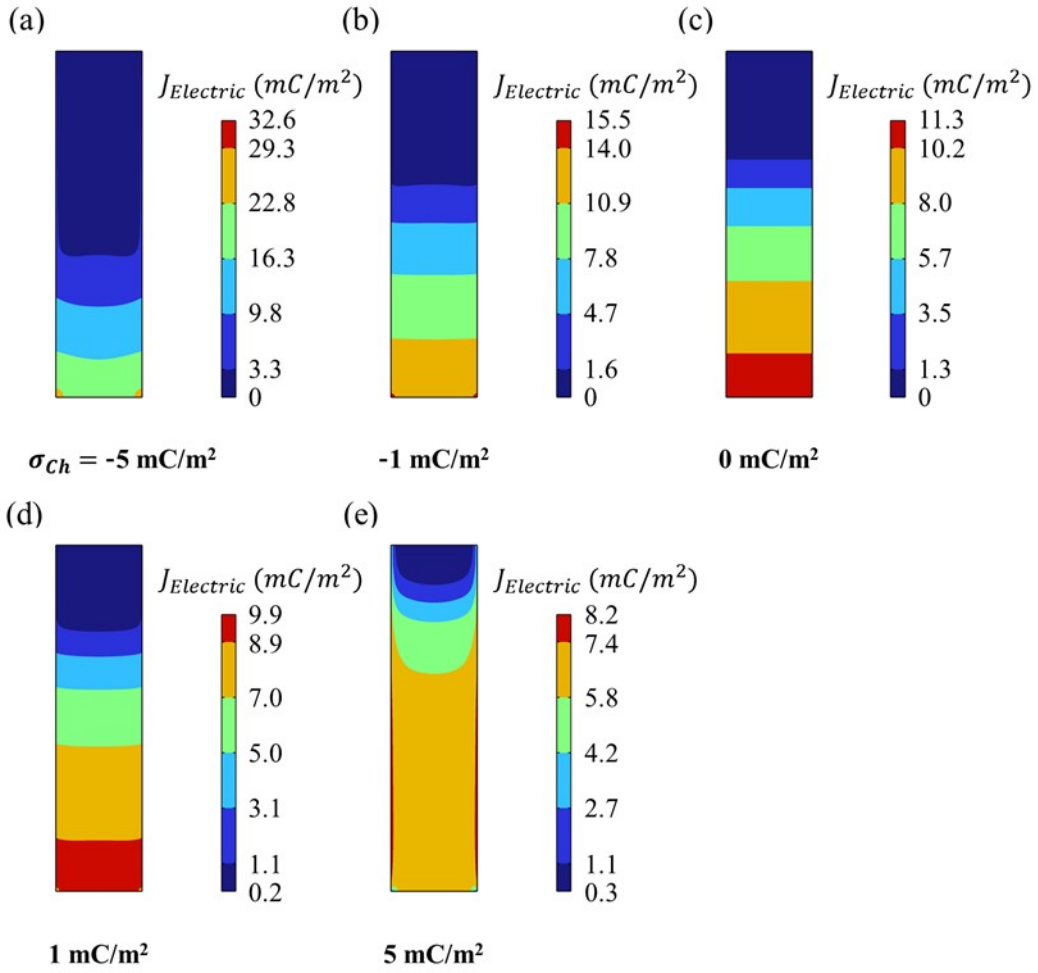

Figure S12. The contour plots of J_{Electric} through the model channel at σ_{Ch} = (a) -5, (b) -1, (c) 0, (d) 1, and (e) 5 mC/m^2.

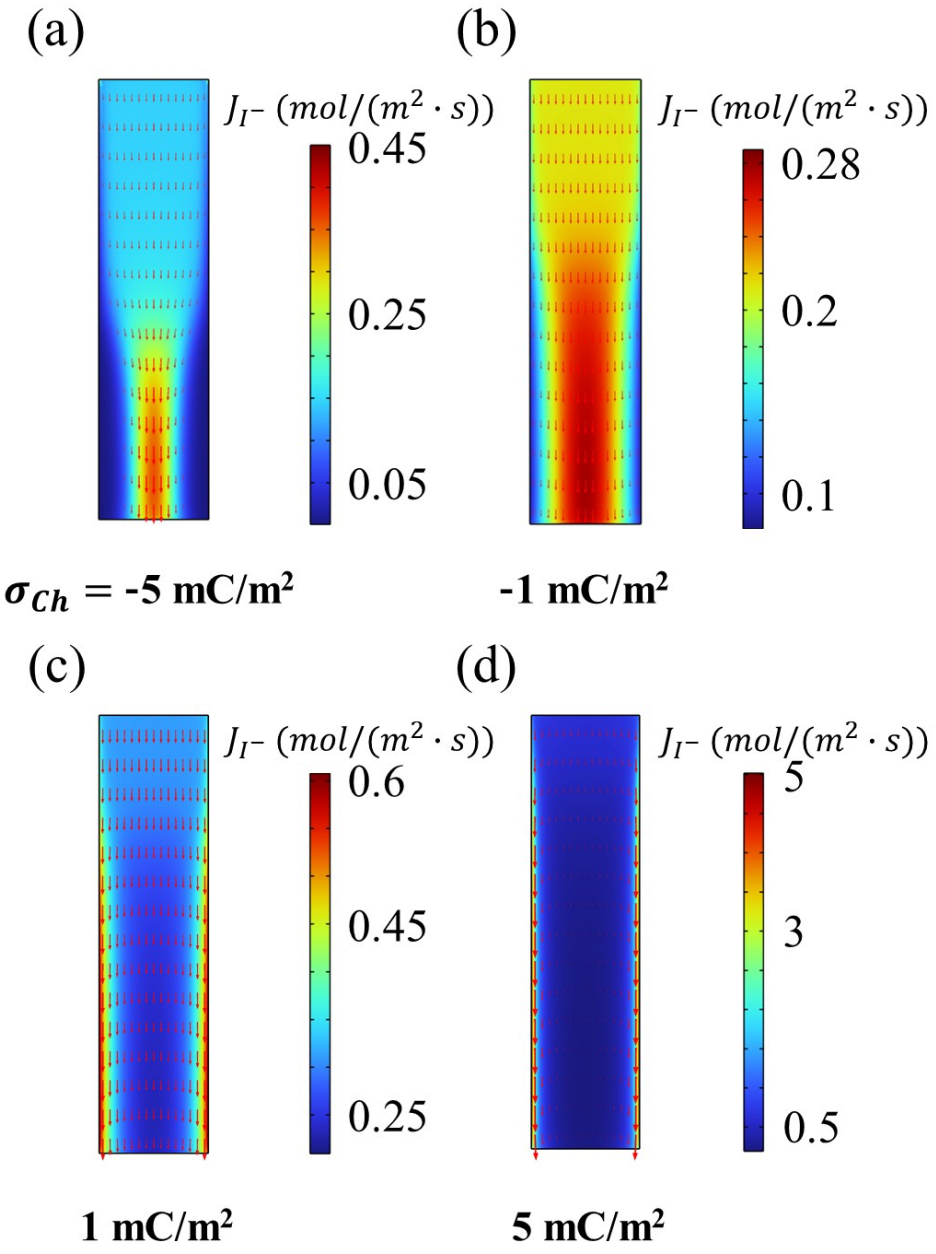

Figure S13. The contour plots of J_I^- through the entire model channel at σ_{Ch} = (a) -5, (b) -1, (c) +1, and (d) +5 mC/m^2; the points and lengths of the arrows designate the directions and the magnitudes of J_I^-.

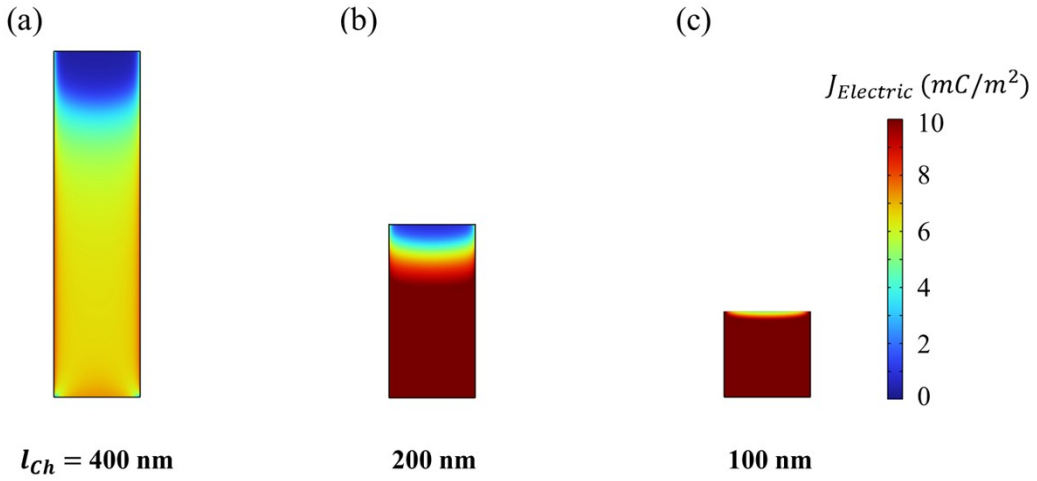

Figure S14. The contour plots of J_{Electric} through the model channel with l_{Ch} = (a) 400, (b) 200, and (c) 100 nm at σ_{Ch} = + 5 mC/m^2 and w_{Ch} = 100 nm.

Note S5. The detailed description of i_{EK} affected by w_{Ch}.

Figure S15 shows the i_{EK}/i_D vs. $\Delta\phi$ plots with different w_{Ch} at σ_{Ch} = +5 mC/m^2. The slope becomes steeper as the channel becomes narrower, and i_{EK}/i_D at $\Delta\phi$ = 3 V with w_{Ch} = 30 nm is approximately twice larger than that with w_{Ch} = 100 nm. The observed current enhancement is explained by J_{I^-} at the electrode with different w_{Ch}, as shown in Figures S16a–c. At w_{Ch} = 100 nm, J_{I^-} between the wall and core of the channel was significantly different. However, J_{I^-} in the channel became more uniformly distributed, while its overall magnitude approached that of the wall as w_{Ch} decreased to 30 nm. These contour plots indicate that the surface conduction of I^- via electrostatic interactions can more significantly affect the electrokinetic transport of I^- through the narrow channel, which is in good agreement with previous reports.[4-6]

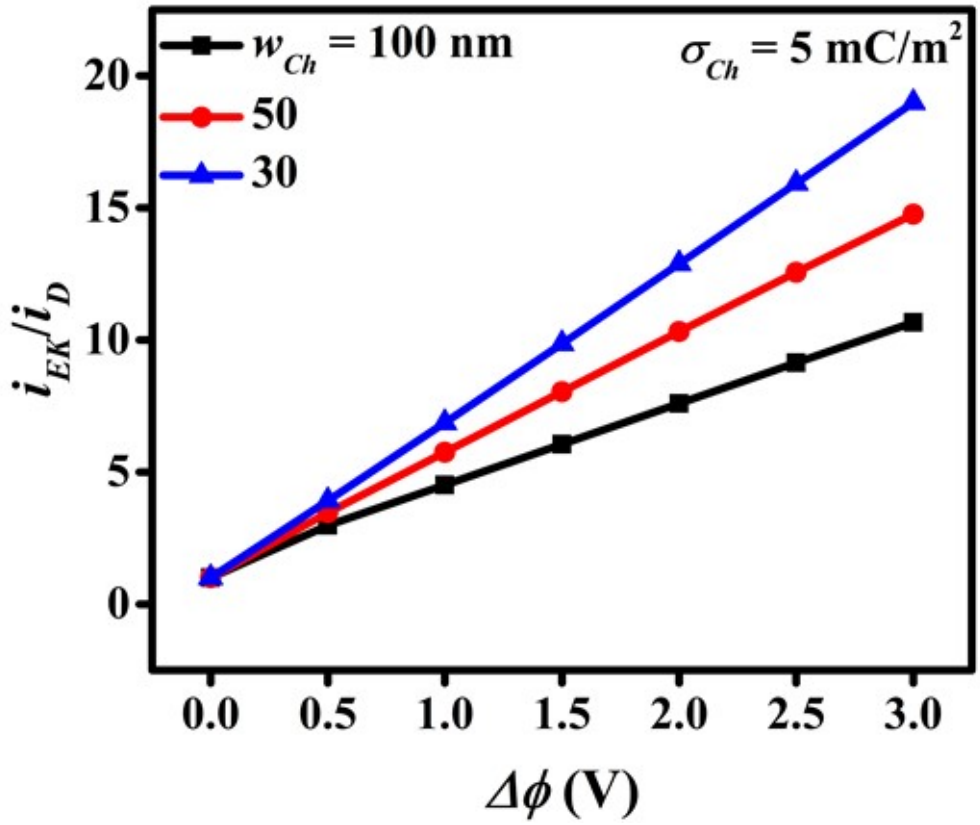

Figure S15. The simulated normalized current (i_{EK}/i_D) vs. $\Delta\phi$ plots at σ_{Ch} = +5 mC/m^2 with w_{Ch} = 30 (blue), 50 (red), and 100 nm (black).

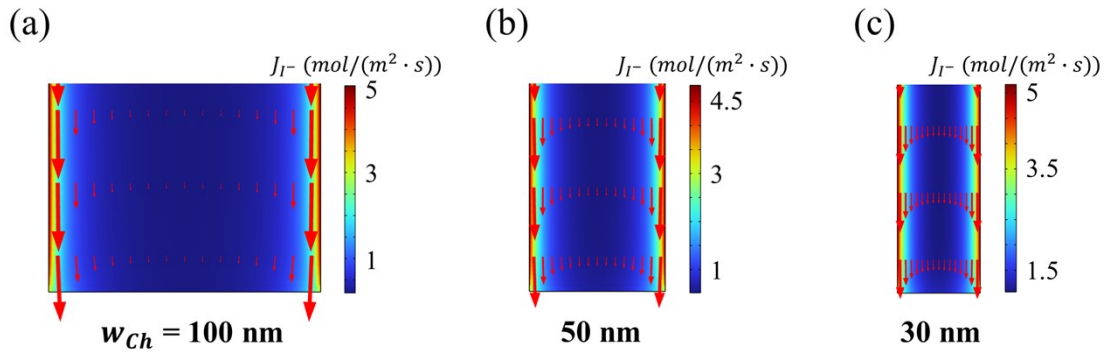

Figure S16. The contour plots of J_{I^-} in the vicinity of the electrode from the model channel at σ_{Ch} = 5 mC/m^2 when w_{Ch} = (a) 100, (b) 50, and (c) 30 nm at l_{Ch} = 400 nm.

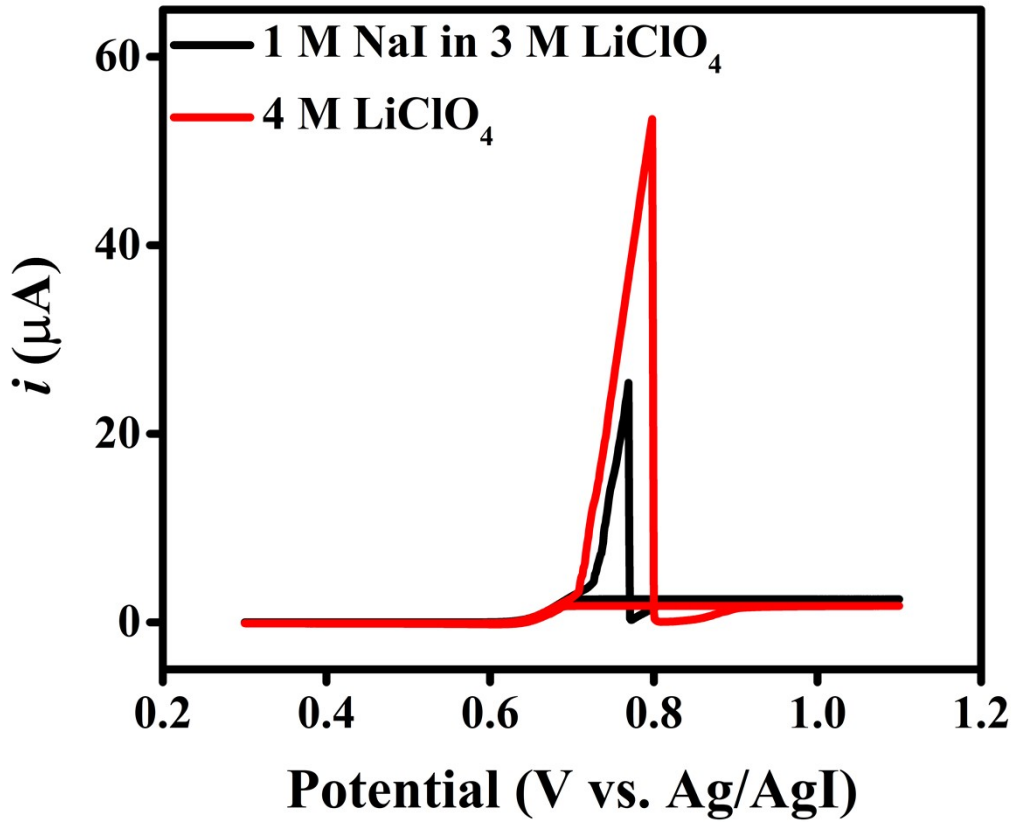

Figure S17. CVs obtained using an aqueous 1 M NaI solutions with $C^{*}_{LiClO_4}$ = 3 M (black) and 4 M (red).

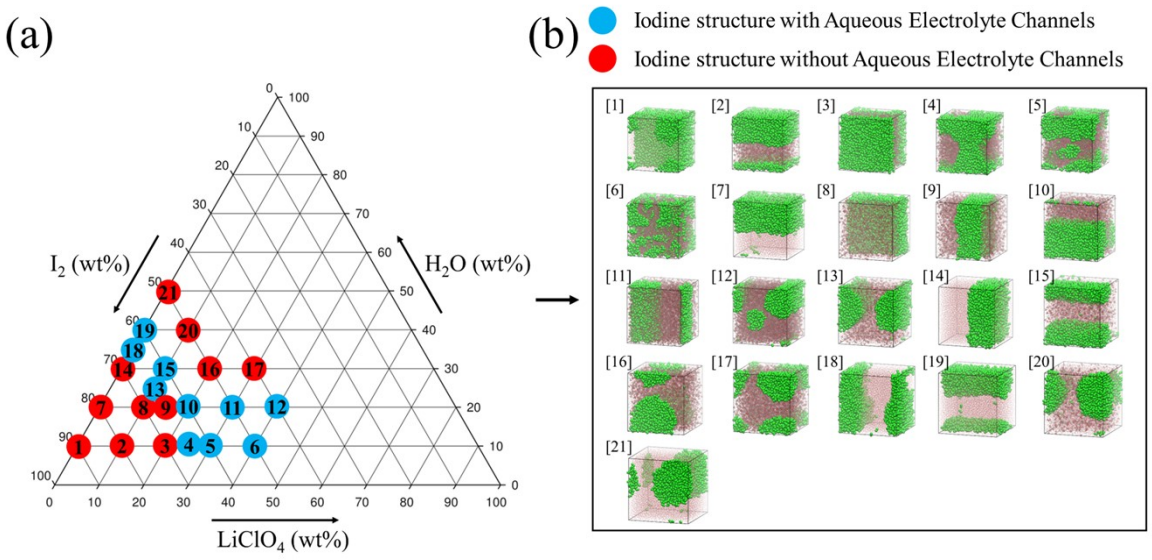

Figure S18. (a) The phase diagrams of I_2 interfacial structures with/without I^--channels as blue and red circles, respectively, at various weight percentages of H_2O, I_2, and $LiClO_4$ estimated from (b) the corresponding MD simulation results; the phases of the iodine structures with the designated numbers were estimated from the MD results with the matched numbers.

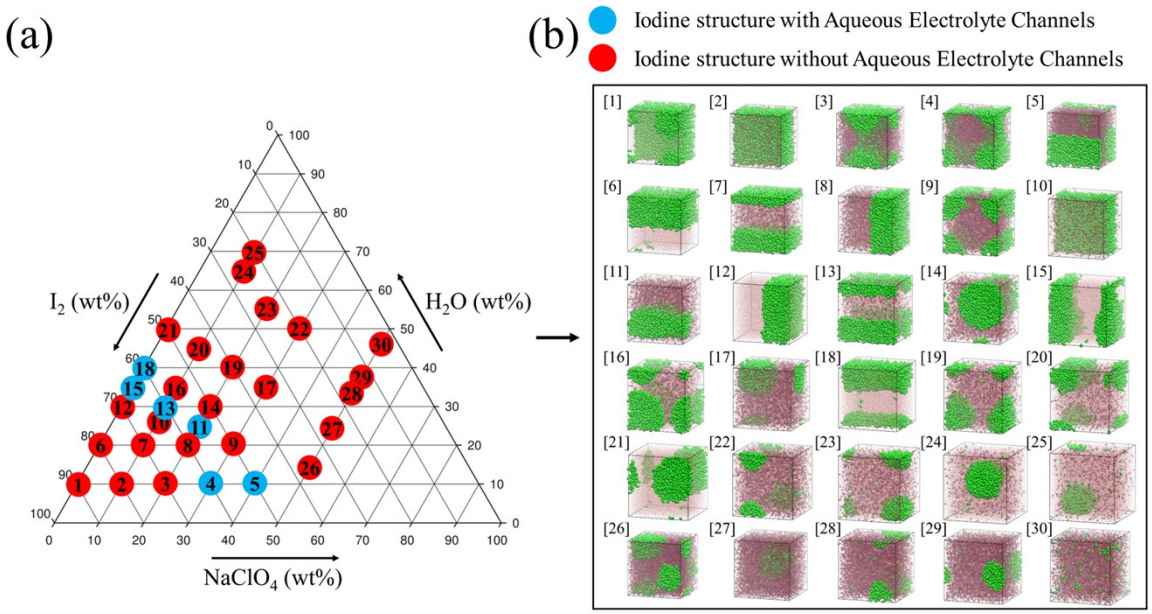

Figure S19. (a) The phase diagrams of I_2 interfacial structures with/without I^--channels as blue and red circles, respectively, at various weight percentages of H_2O, I_2, and $NaClO_4$ estimated from (b) the corresponding MD simulation results; the phases of the iodine structures with the designated numbers were estimated from the MD results with the matched numbers.

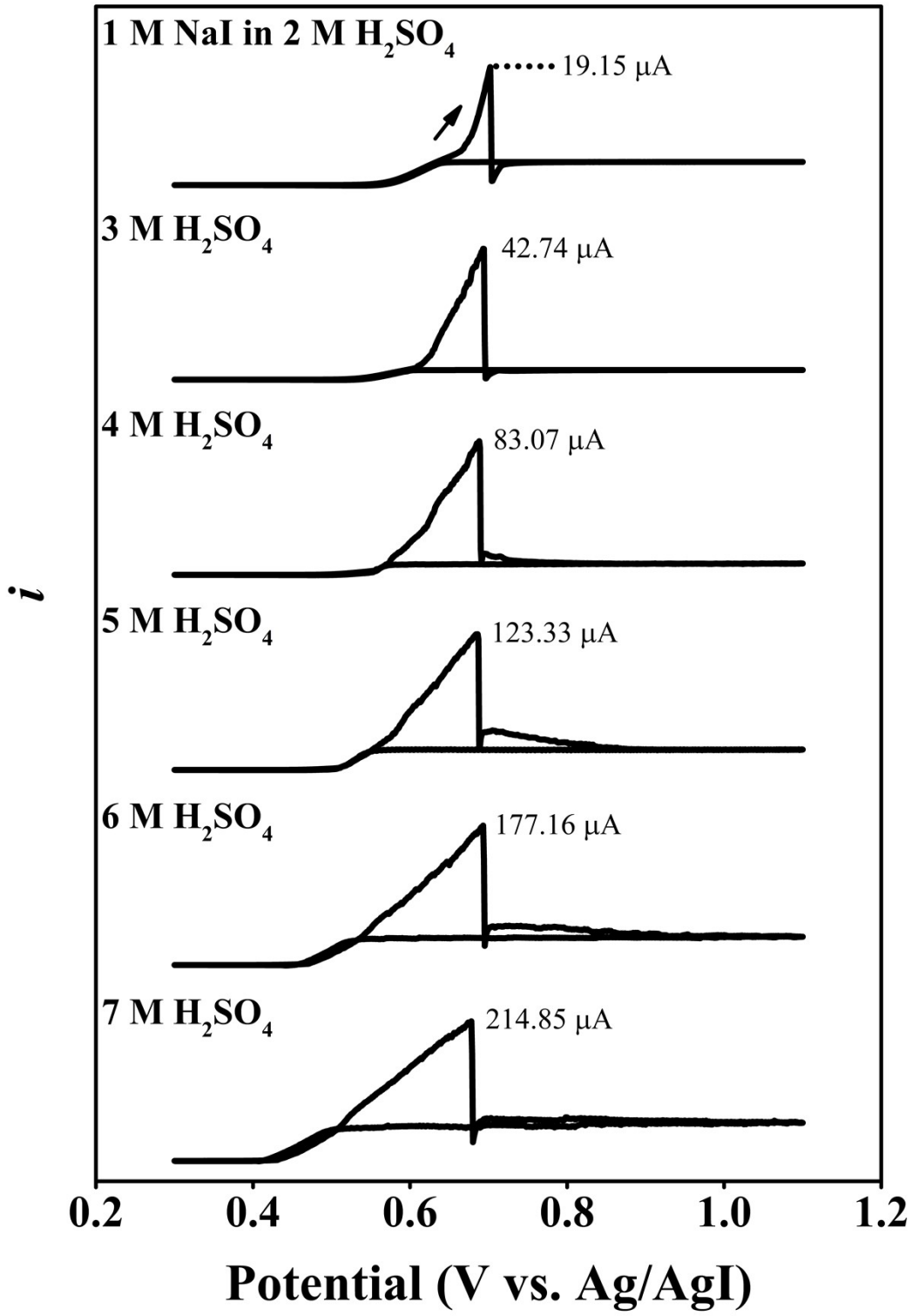

Figure S20. CVs obtained using an aqueous 1 M NaI solutions with $C^{*}_{H_2SO_4}$ from 2 to 7 M.

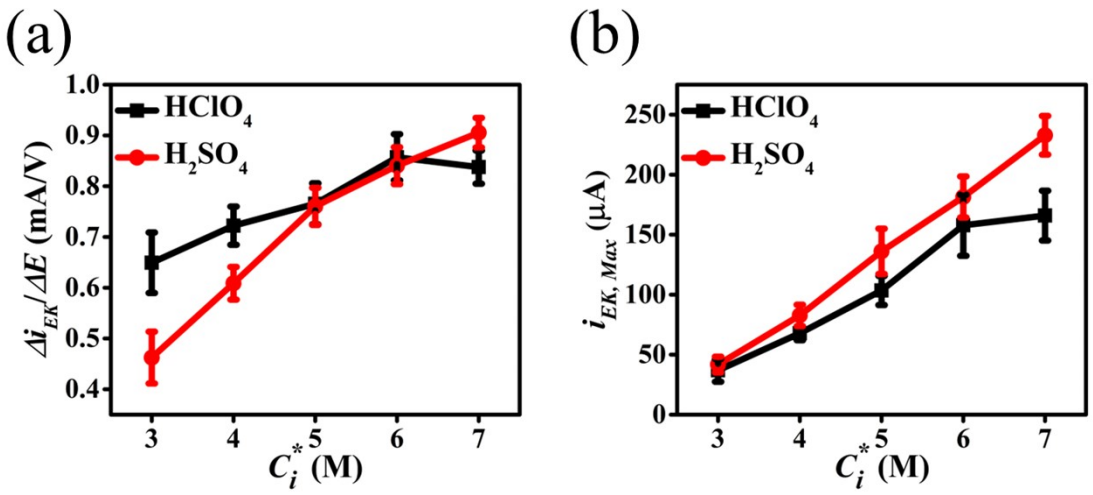

Figure S21. The (a) $\Delta i_{EK}/\Delta E$ and (b) $i_{EK,Max}$ vs. C_i^* plots from the CVs obtained using 1 M NaI solution containing the two different electrolytes (i = $HClO_4$ and H_2SO_4) at varied concentrations.

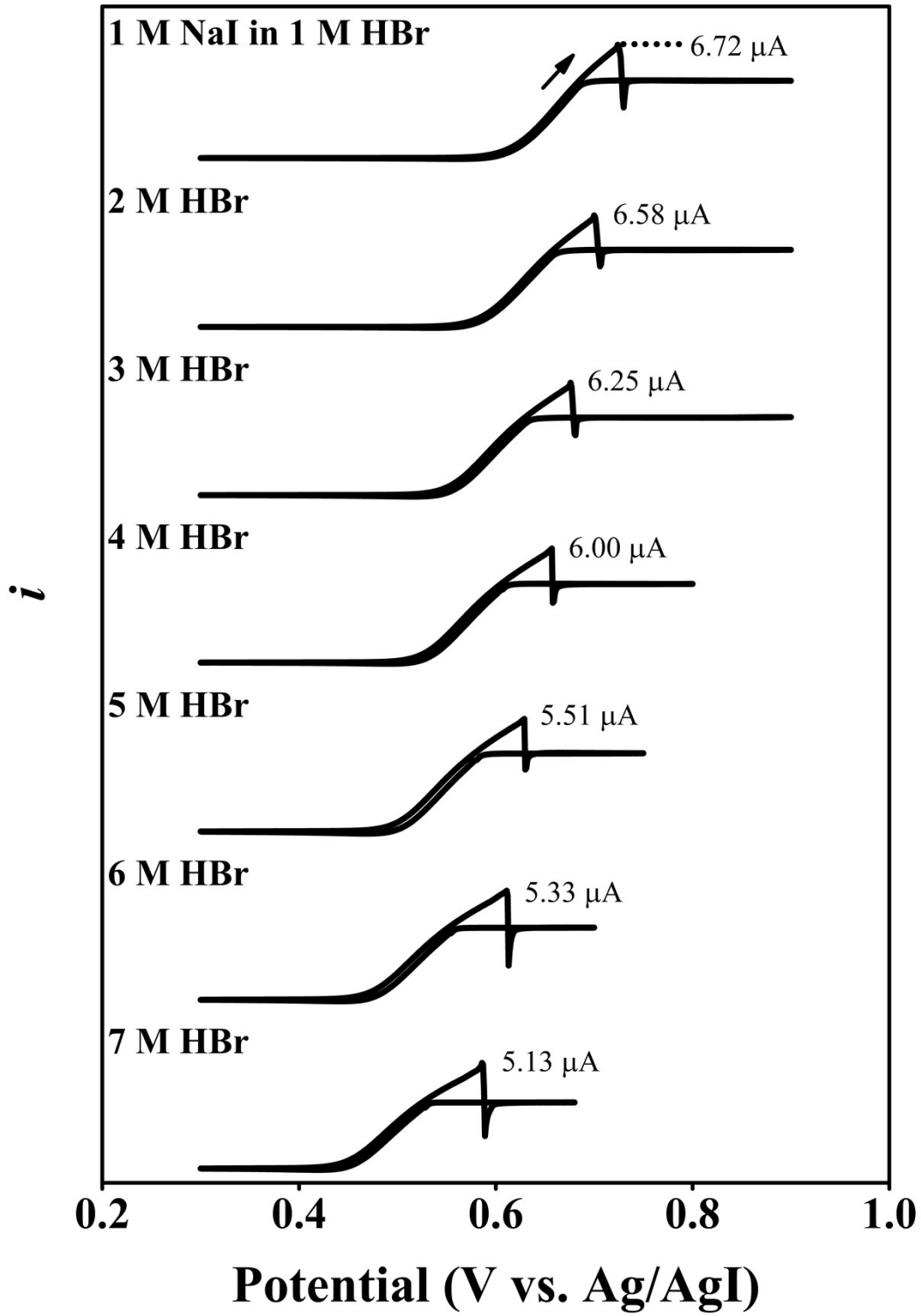

Figure S22. CVs obtained using an aqueous 1 M NaI solution with C^{*}_{HBr} from 1 to 7 M.

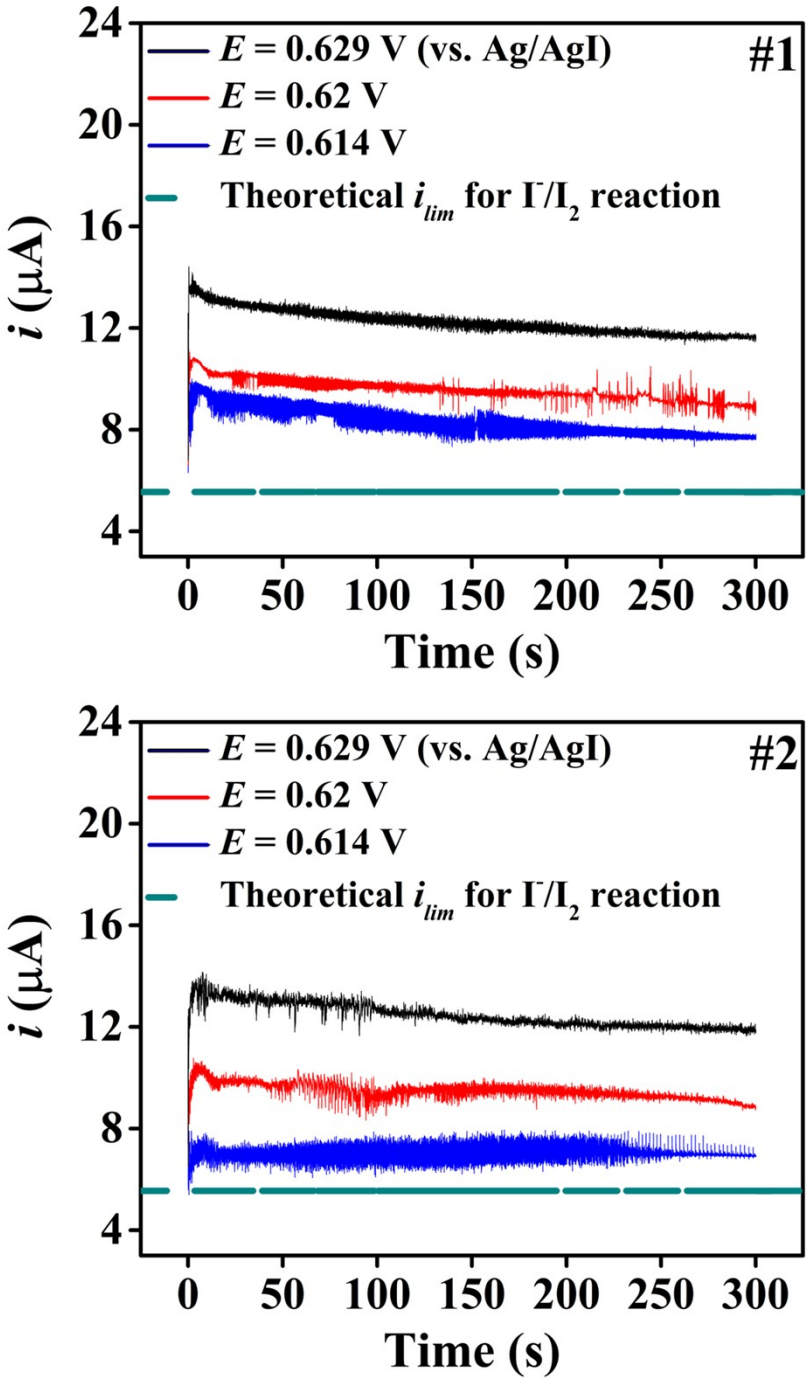

Figure S23. The two sets of *i-t* experiments measured using a Pt UME in an aqueous 1 M NaI solution containing 4 M $HClO_4$ with different electrode potentials; 0.614 (blue), 0.62 (red), and 0.629 (black) for 300 s.

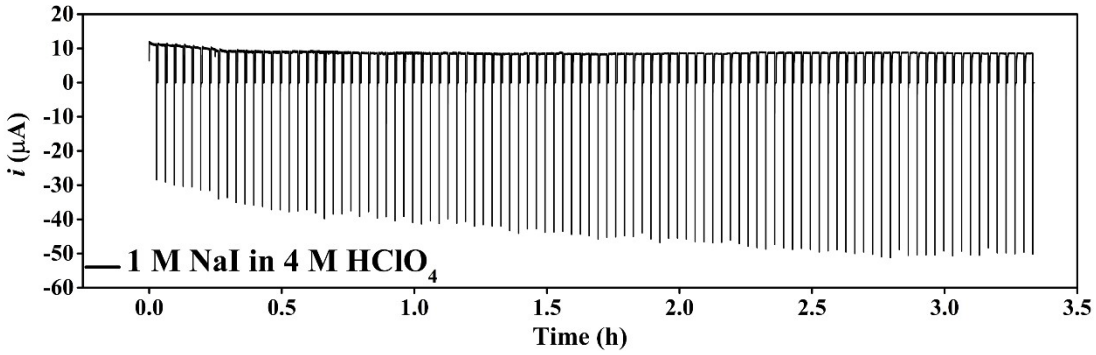

Figure S24. The obtained multi-cycles chronoamperogram (CA) using a Pt UME in an aqueous solution containing 1 M NaI with 4 M $HClO_4$.

Table S1. Room temperature ionic conductivity (σ) of (top) 1 M $HClO_4$ aqueous solutions with different bulk I^- concentrations, $C_{I^-}^*$, and (bottom) 1 M NaI aqueous solutions with different bulk electrolyte conditions, C_i^*. Conductivity of blank spaces in the Table was not obtained due to limited solubility of salts in corresponding conditions in an aqueous solution.

$C_{I^-}^*$	$C_{HClO_4}^*$ = 1 M
1 (mM)	338.2 ± 11.7 (mS/cm)
10	339 ± 7.5
100	343.7 ± 10.1

C_i^* \ i	i = $HClO_4$	$LiClO_4$	$NaClO_4$	H_2SO_4	HCl	HBr
1 (M)	356.7±9.9 (mS/cm)	132.1±1.0	136.9±2.3	415.0±10.8	347.2±5.3	367.5±3.5
2	536.4±15.4	163.8±0.7	170.5±2.6	620.0±14.8	537.0±6.2	562.6±5.6
3	636.3±20.9	182.6±1.3	187.1±2.9	709.1±3.4	659.8±8.7	677.2±8.1
4	664.7±15.5	188.2±1.0	190.4±2.2	720.2±8	730.8±4.2	724.4±6.2
5	638.7±21		181.4±2.3	669.9±6.7	758.2±3.7	733.4±4.4
6	583.9±17.1		165.4±2.7	603.4±15.8		720.4±6.7
7	508±18		144.3±2.2	515.8±20.7		684±8.9
8			121.1±1.8			

Table S2. The number of simulated molecules (right) for each weight percentage condition (left).

H_2O (wt%)	I_2 (wt%)	H_3OClO_4 (wt%)	H_2O	I_2	H_3O^+/ClO_4^-
20	70	10	8882	2206	675
30	60	10	13323	1891	675
40	50	10	17764	1576	675
10	70	20	4441	2206	1351
20	60	20	8882	1891	1351
30	50	20	13323	1576	1351
10	60	30	4441	1891	2026
20	50	30	8882	1576	2026
10	50	40	4441	1576	2701
35	65	0	15543	2049	0
25	65	10	11102	2049	675
10	80	10	4441	2522	675
20	65	15	8882	2049	1013
10	75	15	4441	2364	1013

H_2O (wt%)	I_2 (wt%)	$LiClO_4$ (wt%)	H_2O	I_2	Li^+/ClO_4^-
20	70	10	8882	2206	745
30	60	10	13323	1891	745
40	50	10	17764	1576	745
10	70	20	4441	2206	1490
20	60	20	8882	1891	1490
30	50	20	13323	1576	1490
10	60	30	4441	1891	2235
20	50	30	8882	1576	2235
10	50	40	4441	1576	2979
25	65	10	11102	2049	745
10	80	10	4441	2522	745
20	65	15	8882	2049	1117
10	75	15	4441	2364	1117
10	40	50	4441	1261	3724
20	40	40	8882	1261	2979
10	65	25	4441	2049	1862

30	40	30	13323	1261	2235

H_2O (wt%)	I_2 (wt%)	$NaClO_4$ (wt%)	H_2O	I_2	Na^+/ClO_4^-
70	20	10	31087	630	653
30	60	10	13323	1891	653
20	70	10	8882	2206	653
45	45	10	19984	1418	653
27	63	10	11991	1986	653
63	27	10	27978	851	653
10	70	20	4441	2206	1307
56	24	20	24870	756	1307
40	40	20	17764	1261	1307
24	56	20	10658	1765	1307
10	60	30	4441	1891	1960
49	21	30	21761	662	1960
35	35	30	15543	1103	1960
21	49	30	9326	1544	1960
30	20	50	13323	630	3267
34	16	50	15099	504	3267
38	12	50	16876	378	3267
42	8	50	18652	252	3267
46	4	50	20429	126	3267
35	15	50	15543	473	3267
25	25	50	11102	788	3267
15	35	50	6661	1103	3267
10	80	10	4441	2522	653
40	60	0	17764	1891	0
10	60	30	4441	1891	1960
35	55	10	15543	1734	653
30	70	0	13323	2206	0
50	50	0	22205	1576	0
30	50	20	13323	1576	1307
10	50	40	4441	1576	2614
20	60	20	8882	1891	1307
20	80	0	8882	2522	0
10	90	0	4441	2837	0

Table S3. The domain and boundary conditions used for the finite element analysis, as described in Note S2 using the domain shown in Figure S3.

Domain or Boundary	Nernst-Planck
Domain	$C_{I_3^-,initial} = C_{I_3^-}^{*}$ [1,2], $C_{I_2,initial} = 0$
B1	$C_{I_3^-} = C_{I_3^-}^{*},\ C_{I_2} = 0$
B2	$-n \cdot J_i = 0$ [3]

[1] $C_{i,initial}$ indicates the initial concentration of *i* chemical species.

[2] $C_{I_3^-}^{*}$ was estimated to 3.3, 33.3 and 333.3 mM for $C_{I^-}^{*}$= 10, 100, and 1000 mM, respectively.

[3] n indicates the surface normal vector.

Table S4. The boundary conditions used in the finite element analyses, as described in Note S3 using the domain shown in Figure S9.

Boundary	Poisson	Nernst-Planck	Navier-Stokes
B1	$\phi = 0\ V$	$C_i = C_i^*$	$[-p\mathrm{I} + \mu(\nabla u + (\nabla u)^T)]\cdot n = 0$[1]
B2	$-n \cdot (\varepsilon_0 \varepsilon_r \nabla \phi) = \sigma_{Ch}$	$-n \cdot (J_i + uC_i) = 0$	$u = 0$
B3	$\phi = \phi_{app}$[2]	$C_i = 0$	$u = 0$

[1] The equation corresponds to zero-normal-stress condition, where I is the identity matrix.

[2] ϕ_{app} was increased from 0 to 3 V in 0.5 V of increments to generate the electrical potential difference ($\Delta\phi$) within the model channel.

References

1. C. Park and J. Chang, *Electrochim. Acta*, 2021, **368**, 137650.
2. A. J. Bard and L. R. Faulkner, *Electrochemical Methods: Fundamentals and Applications*, John Wiley & Sons, Inc., 2001, pp. 168-176.
3. A. J. Bard and L. R. Faulkner, *Electrochemical Methods: Fundamentals and Applications*, John Wiley & Sons, Inc., 2001, pp. 92-107.
4. E. V. Dydek, B. Zaltzman, I. Rubinstein, D. S. Deng, A. Mani and M. Z. Bazant, *Phys. Rev. Lett.*, 2011, **107**, 118301.
5. D. Deng, E. V. Dydek, J.-H. Han, S. Schlumpberger, A. Mani, B. Zaltzman and M. Z. Bazant, *Langmuir*, 2013, **29**, 16167-16177.
6. F. H. J. van der Heyden, D. Stein and C. Dekker, *Phys. Rev. Lett.*, 2005, **95**, 116104.